GeoScienceWorld
Lithosphere
Volume 2022, Article ID 1409110, 16 pages
https://doi.org/10.2113/2022/1409110

Lithosphere

Research Article

A Three-Dimensional Constitutive Model for Rocks Based on a Strain-Dependent Elastic Modulus

Z. Li,[1] **Y. Fujii**,[1] **J. Kodama**,[1] **D. Fukuda**,[1] **A. B. N. Dassanayake**,[2] **and P. Sinkala**[1]

[1]*Rock Mechanics Laboratory, Division of Sustainable Resources Engineering, Graduate School of Engineering, Hokkaido University, Sapporo 060-8628, Japan*
[2]*Department of Earth Resources Engineering, University of Moratuwa, Moratuwa 10400, Sri Lanka*

Correspondence should be addressed to Z. Li; zhaoxin.li.w5@elms.hokudai.ac.jp

Received 22 December 2021; Accepted 20 August 2022; Published 5 September 2022

Academic Editor: Songjian Ao

Copyright © 2022 Z. Li et al. Exclusive Licensee GeoScienceWorld. Distributed under a Creative Commons Attribution License (CC BY 4.0).

Our research group previously proposed a simple two-dimensional (2D) constitutive model for rocks to simulate not only the axial stress–axial strain relationship, but also the axial stress–lateral strain relationship, with few complicated equations. However, the failure envelope that it predicted was linear, and it did not consider the effect of the intermediate principal stress (σ_2). In the present study, the authors modify this simple 2D model to have a convex failure criterion. Then, the model is extended to a simple three-dimensional (3D) model that well approximates true triaxial stress–strain curves for real rocks under specific values of σ_2 and σ_3 and uses only four parameters. However, the predicted peak stress–σ_2 relationship is linear. Finally, a modified 3D model was developed, which exhibited the true triaxial convex failure criterion. The equations in this model are simpler than the conventional true triaxial failure criteria. The proposed models can be implemented with a finite element method to improve the design of rock structures.

1. Introduction

A 3D constitutive model is required for the analysis of rock structures. However, as shown below, complex equations are used just to represent the true triaxial strength. This paper aims to develop a 3D constitutive model which is simple and can fairly represent the deformation and failure of rocks under the effects of the intermediate principal stress. The model would contribute to better rock structure design if combined with 3D numerical stress software.

The simplest three-dimensional (3D) constitutive model for rocks is

$$\sigma_1 = (\lambda + 2\mu)\varepsilon_1 + \lambda\varepsilon_2 + \lambda\varepsilon_3, \quad (1)$$

$$\sigma_2 = \lambda\varepsilon_1 + (\lambda + 2\mu)\varepsilon_2 + \lambda\varepsilon_3, \quad (2)$$

$$\sigma_3 = \lambda\varepsilon_1 + \lambda\varepsilon_2 + (\lambda + 2\mu)\varepsilon_3, \quad (3)$$

where ε_1, ε_2, and ε_3 are the maximum (axial), intermediate, and minimum (lateral) principal strains, respectively; σ_1, σ_2, and σ_3 are the maximum (axial), intermediate, and minimum (lateral) principal stresses, respectively, and λ and μ are Lame's constants (Figures 1(a) and 1(b)).

Elasto-brittle models can be derived by introducing peak and residual strengths (Figures 1(c) and 1(d)). However, the resulting stress–strain curves, which should be curvilinear for real rocks, are unrealistic polylines. More realistic stress–strain curves, which are needed for precise analyses of rock structures, can be obtained using various two-dimensional (2D) constitutive models [1–14].

A variable-compliance-type constitutive model [7] is (Figure 2)

$$\sigma_1 = \left(\frac{\omega}{b}\right)^{1/(n-3)} \varepsilon_1^{-m/(n-m)}, \quad (4)$$

where $\omega = d\psi/dt$, $\psi = \varepsilon_1/\sigma_1$, and n, m, and b are constants. This equation simulates the axial stress–axial strain relationships for classes I and II. However, no reasonable methods to evaluate the lateral strain have yet been provided. Actual

Downloaded from http://pubs.geoscienceworld.org/gsa/lithosphere/article-pdf/doi/10.2113/2022/1409110/5686341/1409110.pdf
by guest

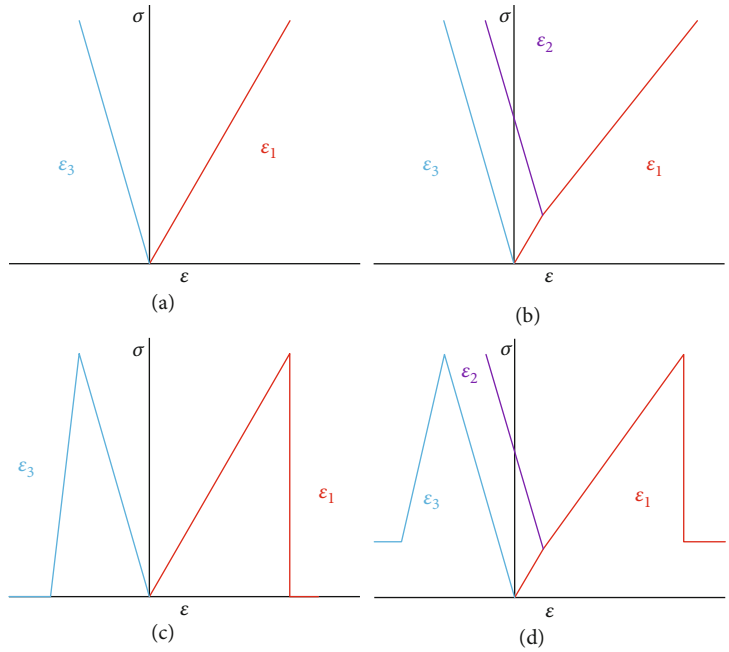

Figure 1: The simplest 3D constitutive model under (a) uniaxial compression and (b) $\sigma_2 > \sigma_3$. A 3D elasto-brittle model under (c) uniaxial compression and (d) $\sigma_2 > \sigma_3$.

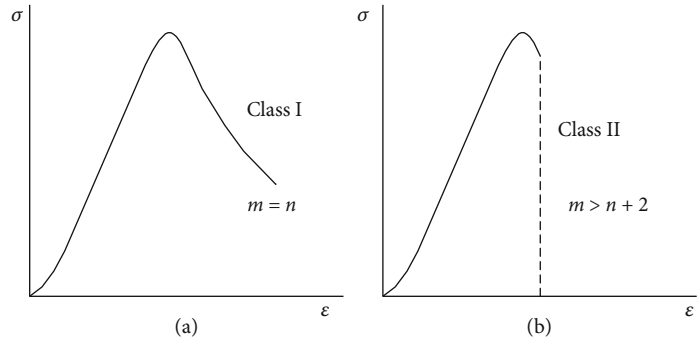

Figure 2: A variable-compliance-type constitutive model [7].

rocks under compression show lateral dilatancy around peak stress in most cases, due to the growth of axial microcracks [15–18]; this growth is essential to the deformation and failure of rocks [19]. Therefore, the axial stress–lateral strain relationship is more important than the axial stress–axial strain relationship [20, 21].

By contrast, a simple 2D constitutive model for rocks was proposed by our research group [22] based on the finding that the trace of the axial strain, lateral strain, and axial stress is located on a plane in a 3D coordinate system for rocks such as Paleogene Kamisunagawa sandstone (Figure 3, [22]), Cretaceous Pombetsu sandstone, Paleogene Bibai sandstone, and Paleogene Inada granite [23]. The equations in the model are very simple, and class I and II strain-softening behaviors can be obtained with appropriate lateral strain behavior by introducing the strain-dependent elastic modulus.

For the 3D case, the strength of rocks is affected by σ_2 ([24–27], and [28–32], Figure 4; [33]), and various criteria have been proposed to describe these effects ([25–27], and [30, 34–43]). These criteria use complicated equations and many parameters. For example, a modified Lade criterion proposed by Ewy [44] (Figure 5(a)) is represented as

$$\frac{\left(I_1'\right)^3}{I_3'} = 27 + \eta, \tag{5}$$

$$I_1' = (\sigma_1 + s_1 - p_0) + (\sigma_2 + s_1 - p_0) + (\sigma_3 + s_1 - p_0), \tag{6}$$

$$I_3' = (\sigma_1 + s_1 - p_0) + (\sigma_2 + s_1 - p_0) + (\sigma_3 + s_1 - p_0), \tag{7}$$

where p_0 is pore pressure, η is related to the internal friction, and s_1 represents the cohesion of the rock. The peak strength

Downloaded from http://pubs.geoscienceworld.org/gsa/lithosphere/article-pdf/doi/10.2113/2022/1409110/5686341/1409110.pdf
by guest

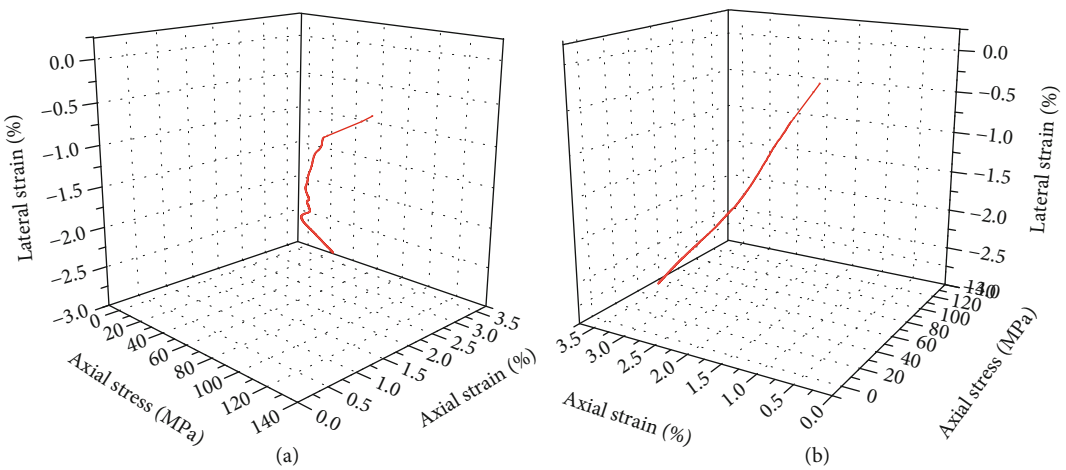

Figure 3: 3D plots of strains and axial stress under uniaxial compression; after rotating the coordinate system, the originally curvilinear trace (a) appears as a straight line (b).

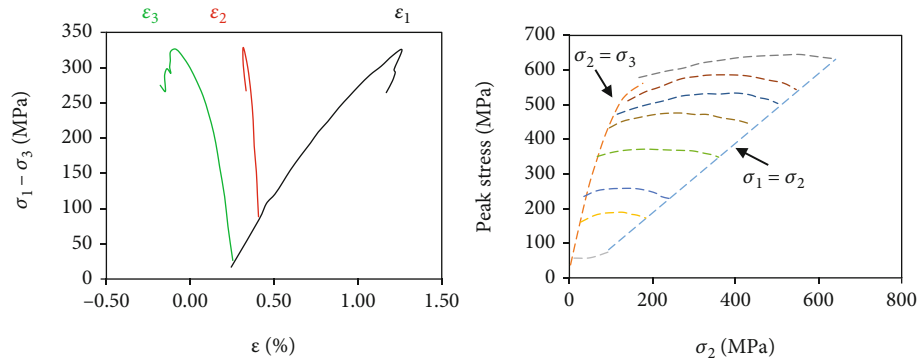

Figure 4: True triaxial test results of Coconino sandstone [29].

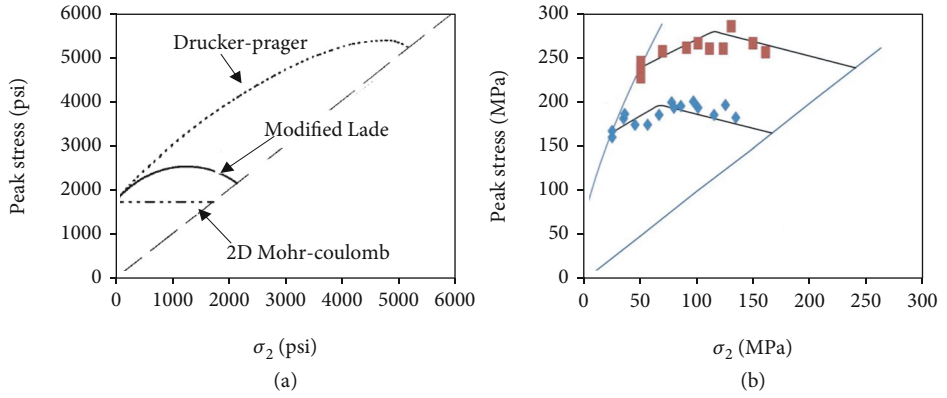

Figure 5: (a) Modified Lade criterion by $s_0 = 500$ Psi, $\varphi = 30°$, and $\sigma_3 = 0$ [44]. (b) 3D HB criterion for Yuubari shale [38].

first increases and then decreases with σ_2 according to the modified Lade criterion.

As another example, a 3D failure criterion for rocks proposed by Li et al. [38] based on the Hoek–Brown criterion [45, 46] is expressed as

$$\sigma_1 = \frac{b\sigma_2 + \sigma_3}{b+1} + \sigma_c\left(\frac{m_b}{\sigma_c}\frac{b\sigma_2 + \sigma_3}{b+1} + s\right)^{\alpha} (\text{low}\sigma_2), \quad (8)$$

$$\frac{b\sigma_2 + \sigma_1}{b+1} = \sigma_3 + \sigma_c\left(\frac{m_b}{\sigma_c}\sigma_3 + s\right)^{\alpha} (\text{high}\sigma_2), \quad (9)$$

where σ_c and b are the unconfined compressive strength and a constant, respectively, and

$$m_b = \exp\left(\frac{\text{GSI} - 100}{28 - 14D}\right) m_i, \quad (10)$$

Downloaded from http://pubs.geoscienceworld.org/gsa/lithosphere/article-pdf/doi/10.2113/2022/1409110/5686341/1409110.pdf
by guest

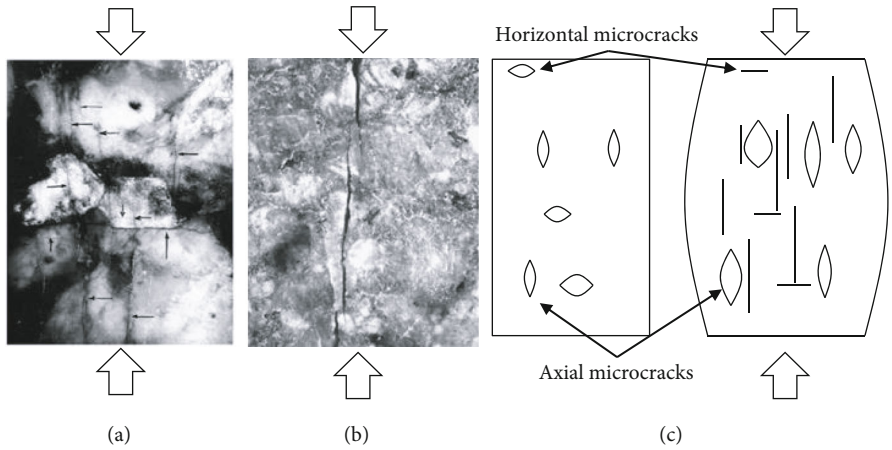

Figure 6: (a) Cracks generated in the uniaxial compression test (vertical loading direction) in granite. The arrows are drawn perpendicular to the cracks. Note that most cracks are parallel to the loading direction [18]. (b) Axial cracks generated in uniaxial compression test in granite [17]. (c) Illustration of axial microcrack initiation and growth and horizontal microcrack closure.

$$s = \exp\left(\frac{\mathrm{GSI} - 100}{9 - 3D}\right), \tag{11}$$

$$\alpha = \frac{1}{2} + \frac{1}{6}\left(e^{-\mathrm{GSI}/15} - e^{-20/3}\right), \tag{12}$$

where m_i, GSI, and D are the material constant for intact rock, geological strength index, and disturbance factor, respectively. The effects of σ_2 on rock strength are represented well in this model (Figure 5(b)); however, the parameter selection is complex, and the resulting peak stress curves are unrealistic polylines.

No constitutive equations can fully represent true triaxial stress–strain curves considering the effects of σ_2. Therefore, this paper proposes a 3D constitutive model with fewer parameters and consideration of these true triaxial stress-strain curves and convex failure envelopes. Herein, we briefly explain the simple 2D constitutive model of Fujii and Ishijima [22]. Then, this simple model is modified to include the convex failure envelope by introducing stress dependency for an elastic modulus. We give an example of its application to a pressurized thick-walled cylinder under the plane strain condition. Then, the simple 2D model is extended to a simple 3D one. Finally, this 3D model is modified to represent true triaxial stress–strain curves and convex failure envelopes.

2. The Simple 2D Constitutive Model

The simple 2D model developed by our research group should be briefly explained before the 3D models because they were developed based on the 2D model, and it has not been published as a full paper in English in a peer-reviewed journal.

A plane in the axial stress–axial strain–lateral strain space (Figure 3) can be represented as

$$\sigma_1 = A(\varepsilon_1 - \varepsilon_0) + \mathrm{kA}\varepsilon_3, \tag{13}$$

where σ_1, ε_1, and ε_3 are the maximum (axial) principal stress, the maximum (axial) principal strain, and the minimum (lateral) principal strain. A is an elastic modulus, and ε_0 and k are constants; these are equal to $\lambda + 2\mu$, 0, and $\nu/(1-\nu)$, respectively, where ν is Poisson's ratio for a linear elastic medium. Using a function of normal strain, $A'(\varepsilon)$, to replace the constant A, and ignoring the constant ε_0 in Equation (13) for simplicity, we get

$$\sigma_1 = A'(\varepsilon_1)\varepsilon_1 + \mathrm{kA}\varepsilon_3. \tag{14}$$

By analogy, the following equation can be written for σ_3:

$$\sigma_3 = A'(\varepsilon_3)\varepsilon_3 + \mathrm{kA}\varepsilon_1, \tag{15}$$

where σ_3 is the minimum (lateral) principal stress. $A'(\varepsilon)$ should increase and converge to a specific value as ε tends to $+\infty$ (compression). The increase represents the increase in axial elastic modulus (A_A) due to microcrack closure (Figure 6), as illustrated in Figure 7(a). $A'(\varepsilon)$ should also decrease with expansion and should converge to a specific value as ε tends to $-\infty$ (expansion). The decrease represents a decrease in the lateral elastic modulus (A_L) under extension due to the initiation and growth of axial microcracks (Figure 6), as illustrated in Figure 7(b). These assumptions have already been confirmed numerically by a boundary element method combining displacement discontinuity [47] with the body force [49] elements in Fujii and Ishijima [23] and explained by various mechanisms (e.g., Figure 8, [17, 48]).

The following function (Figure 9) was chosen as $A'(\varepsilon)$ to satisfy the above requirements:

$$A'(\varepsilon) = D\left[\tan^{-1}\left\{C\left(\frac{\varepsilon}{\varepsilon_s} + 1\right)\right\} + \frac{\pi}{2}\right] + F, \tag{16}$$

Downloaded from http://pubs.geoscienceworld.org/gsa/lithosphere/article-pdf/doi/10.2113/2022/1409110/5686341/1409110.pdf
by guest

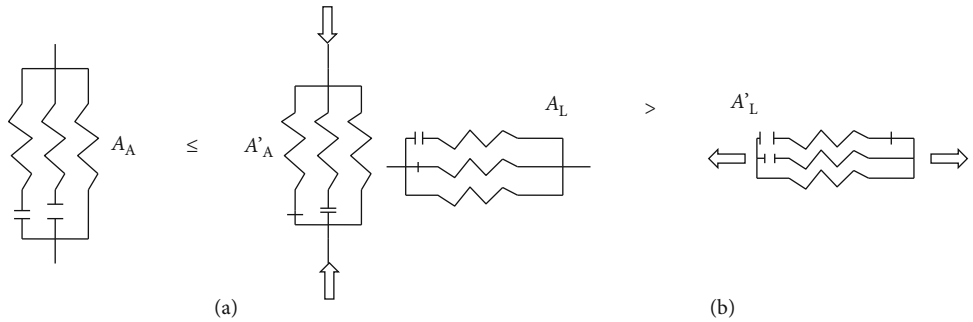

FIGURE 7: (a) Increase in the axial elastic modulus due to compression. (b) Decrease in the lateral elastic modulus due to extension.

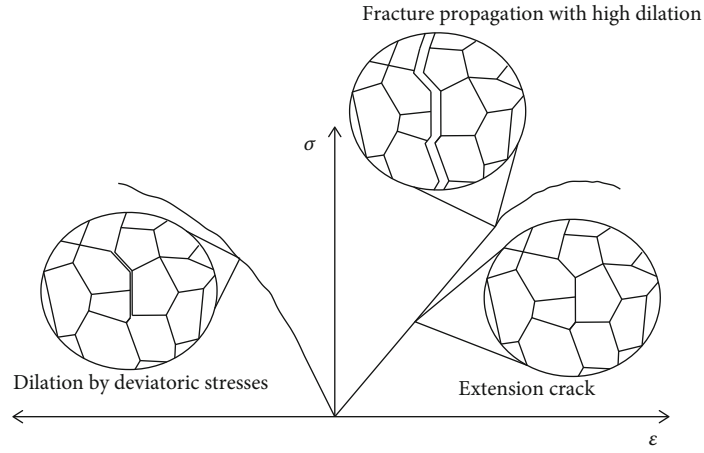

FIGURE 8: Illustration of dilatation by axial microcrack initiation and growth in a laboratory test [17].

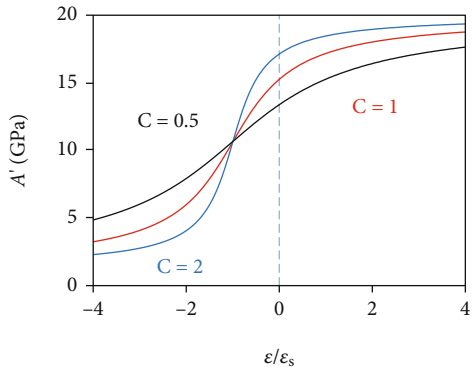

FIGURE 9: Strain-dependent elastic modulus A' for $A = 20$ (GPa) and $k = 0.25$ [22].

$$D = \frac{(1-k^2)A}{\pi}, \tag{17}$$

$$F = k^2 A, \tag{18}$$

where ε_s is a constant whose value is approximately half the absolute value of the critical extensile strain (lateral strain value at the peak load point; [20]), C is a positive constant, and D and F are determined so that the residual strength becomes constant as ε_1 and ε_3 tend to ∞ and $-\infty$, respectively.

From Equations (14) to (18), an ultimate residual strength, σ_{ur}, for infinite strains can be calculated as

$$\sigma_{ur} = \sigma_1(\varepsilon_1 = \infty, \varepsilon_3 = -\infty) = \frac{\sigma_3}{k}. \tag{19}$$

However, the residual strength σ_r at −4.5% lateral strain (Figure 10(f)), which is higher than the ultimate residual strength, will be used hereafter for convenience.

The simple 2D model requires only four parameters (A, k, C, and ε_s) to simulate classes I and II nonlinear stress–strain behaviors (Figures 10(a)–10(e)), and tensile behavior can also be simulated seamlessly (Figure 10(a)). Curves representing such behavior can be obtained as follows, for example:

(a1) Negative ε_3 increment (extensile) is assigned
(a2) ε_1 is calculated by Equation (15)
(a3) $A'(\varepsilon_1)$ and $A'(\varepsilon_3)$ are calculated by Equation (16)
(a4) σ_1 can be calculated by Equation (14)
(a5) Iterate steps (a2–a4) until the solution converges
(a6) Iterate steps (a1–a5) for loading until ε_3 reaches -0.045

It is rather surprising that only a decrease in the lateral elastic modulus can induce strain-softening behavior. The mechanism of the strain softening is as follows. The elastic modulus $A'(\varepsilon_3)$ decreases with lateral extensile strain, and this strain increases by Equation (15). According to Equation

Downloaded from http://pubs.geoscienceworld.org/gsa/lithosphere/article-pdf/doi/10.2113/2022/1409110/5686341/1409110.pdf
by guest

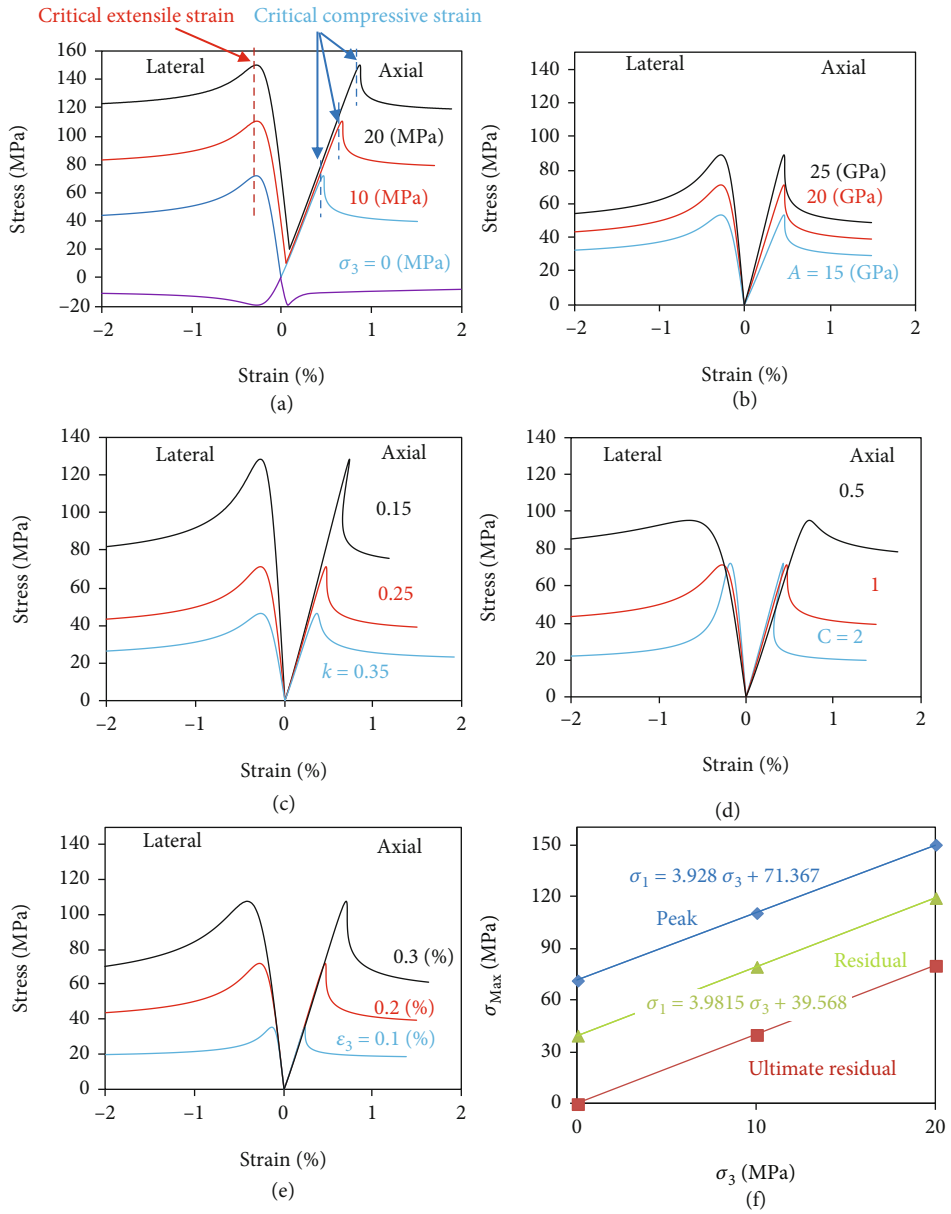

FIGURE 10: Simulated stress-strain curves by Equations (14)–(18). Default values are $A = 20$ (GPa), $k = 0.25$, $C = 1$, $\varepsilon_s = 0.002$, and $\sigma_3 = 0$. (a) Effects of σ_3. (b) Effects of A. (c) Effects of k. (d) Effects of C. (e) Effects of ε_s. (f) Failure envelopes for Figure 10(a).

(14), the lateral extensile strain increment causes a decrease in axial stress. The peak load point appears when the stress increase due to the axial strain increment becomes the same as the stress decrease due to the lateral extensile strain increment. In step (a1), the axial strain increment can be assigned instead of the lateral extensile strain one to simulate class I behavior.

Considering the model's parameters, A mainly affects strength and tangent modulus (Figure 10(b)). k mainly affects strength, the shape of the $\sigma_1 - \varepsilon_1$ curve around the peak load, Poisson's ratio, and the critical compressive strain (ε_1 value at the peak load point; [20]; Figure 10(c)). C mainly affects the shape of the stress–strain curves around the peak load, strength, and the critical strains (Figure 10(d)). ε_S mainly affects the critical strains and strength (Figure 10(e)).

One of the limitations of this model is that it predicts a linear failure envelope (Figure 10(f)). Therefore, we modify it in the next chapter. However, other results are similar to real rocks:

(i) Compressive strength increases with σ_3 (Figure 10(a))

(ii) Compressive strength is larger than tensile strength (Figure 10(a))

(iii) Critical compressive strain increases with σ_3 (Figure 10(a), [20])

(iv) Critical extensile strain is unaffected by σ_3 (Figure 10(a), [20])

Downloaded from http://pubs.geoscienceworld.org/gsa/lithosphere/article-pdf/doi/10.2113/2022/1409110/5686341/1409110.pdf
by guest

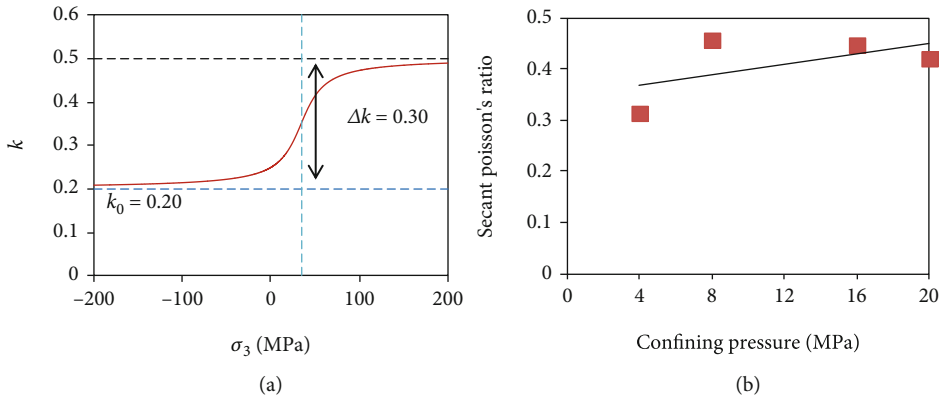

FIGURE 11: (a) Confining pressure-dependent k in the case where $k_0 = 0.20$, $\sigma_0 = 35$ MPa, $\alpha = 20$ MPa, and $\Delta k = 0.30$. (b) Secant Poisson's ratio increases with confining pressure for Kamisunagawa sandstone [22, 23].

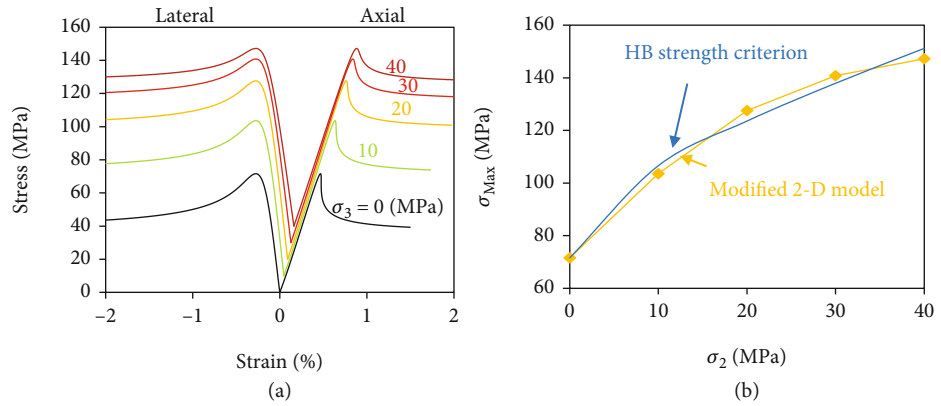

FIGURE 12: Stress-strain curves. (a) Stress-strain curves. (b) Failure envelope.

3. Modified 2D Model

3.1. Introduction of k Dependent on Confining Pressure. We introduce k dependent on confining pressure (Figure 11(a)) to give a convex failure envelope based on the increase in the secant Poisson's ratio with confining pressure under triaxial compression (Figure 11(b)):

$$k = \frac{\Delta k}{\pi}\left[\tan^{-1}\left\{\frac{1}{\alpha}(\sigma_3 - \sigma_0)\right\} + \frac{\pi}{2}\right] + k_0, \qquad (20)$$

where k_0 is the minimum value, Δk is the amplitude, and σ_0 and α are constants. The ultimate residual strength is unchanged from Equation (19).

The stress–strain curves obtained by setting default values of $A = 20$ GPa, $C = 1$, $\varepsilon_s = 0.002$, $k_0 = 0.20$, $\sigma_0 = 35$ MPa, $\alpha = 20$ MPa, and $\Delta k = 0.30$ show strain-softening behaviors (Figure 12(a)) with a convex failure envelope (Figure 12(b)). The stress drop decreases, and the strain-softening behavior becomes mild as confining pressure increases; these are common features of rock deformation. Figure 12(b) also shows the failure envelope predicted by the Hoek–Brown strength criterion with $\sigma_c = 71.6$ MPa, $m_b = 119.0$, $s = 1$, and $\alpha = 0.104$, which is similar. Therefore, the equations are expected to approximate the stress–strain curves and convex failure envelope of various rocks. Considering the model parameters, k_0 mainly affects the maximum stress (Figure 13(a)). Δk (Figure 13(b)) and σ_0 (Figure 13(c)) mainly affect the internal friction angle. α mainly affects the convexity of the failure envelope (Figure 13(d)).

3.2. Approximating Convex Failure Envelope for Test Results. The procedure for approximating ordinary triaxial experimental data using the modified 2D model is as follows:

(b1) Adjust A to approximate the gradient of the stress–strain curve

(b2) Adjust C to approximate the overall shape of each stress–strain curve

(b3) Adjust ε_s to approximate the peak load point and slope of the failure envelope

(b4) Adjust k to approximate the gradient of the axial stress–lateral strain curve and peak strength

(b5) Iterate steps (b1–b4) until the stress–strain curves for the rocks are approximated well

(b6) Adjust k to approximate the peak strength for the triaxial compression test

(b7) Use a nonlinear least squares method for the k vs. σ_3 curve to obtain values of k_0, Δk, α, and σ_0 (e.g., Figures 14 and 15(b))

Downloaded from http://pubs.geoscienceworld.org/gsa/lithosphere/article-pdf/doi/10.2113/2022/1409110/5686341/1409110.pdf
by guest

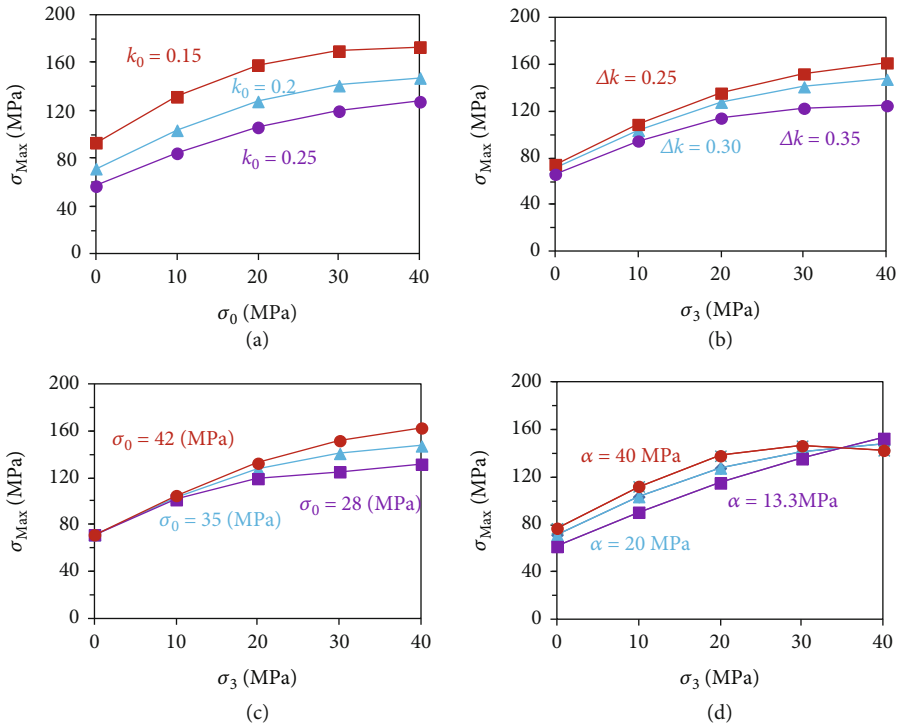

FIGURE 13: Effect of parameters on the failure envelopes. σ_{max} is the maximum principle stress, and σ_3 is the minimum principle stress. (a) Effects of k_0. (b) Effect of Δk. (c) Effect of σ_0. (d) Effect of α.

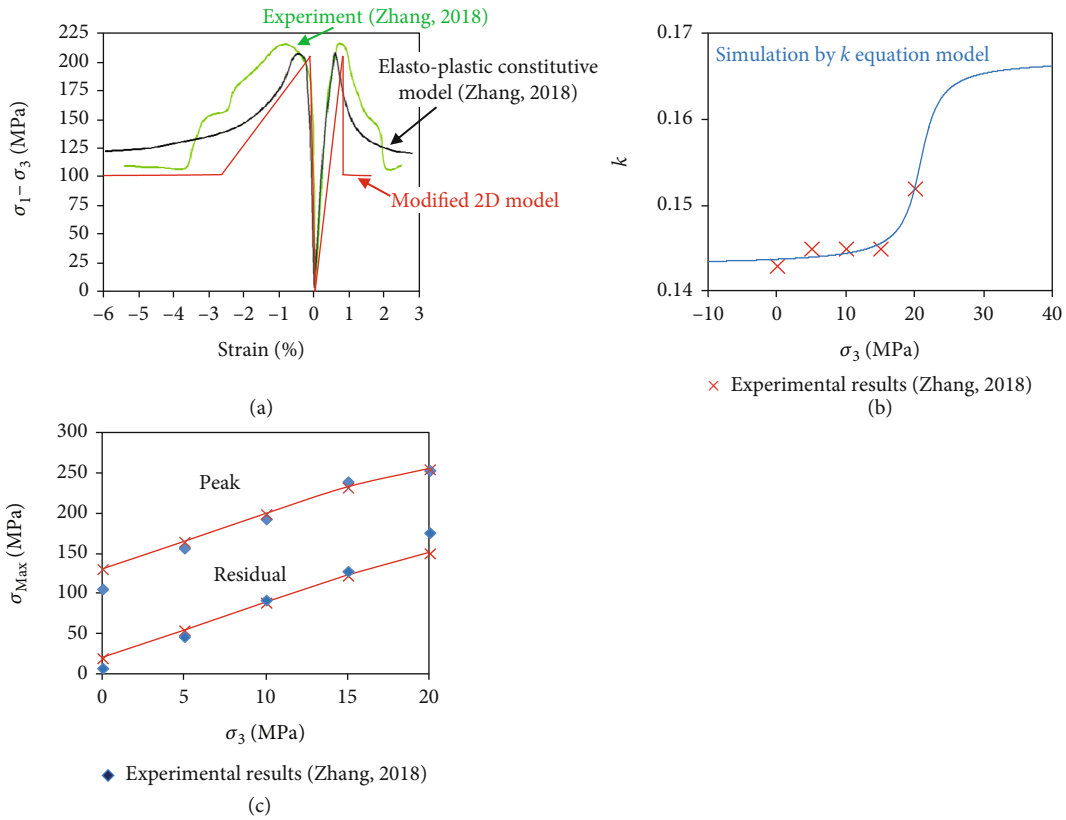

FIGURE 14: (a) Stress-strain curves of limestone under $\sigma_3 = 15$ (MPa). (b) k vs. σ_3 for parameter $A = 27$ (GPa), $C = 3.5$, and $\varepsilon_s = 0.0013$. (c) Approximated convex failure envelopes by modified 2D model.

Downloaded from http://pubs.geoscienceworld.org/gsa/lithosphere/article-pdf/doi/10.2113/2022/1409110/5686341/1409110.pdf
by guest

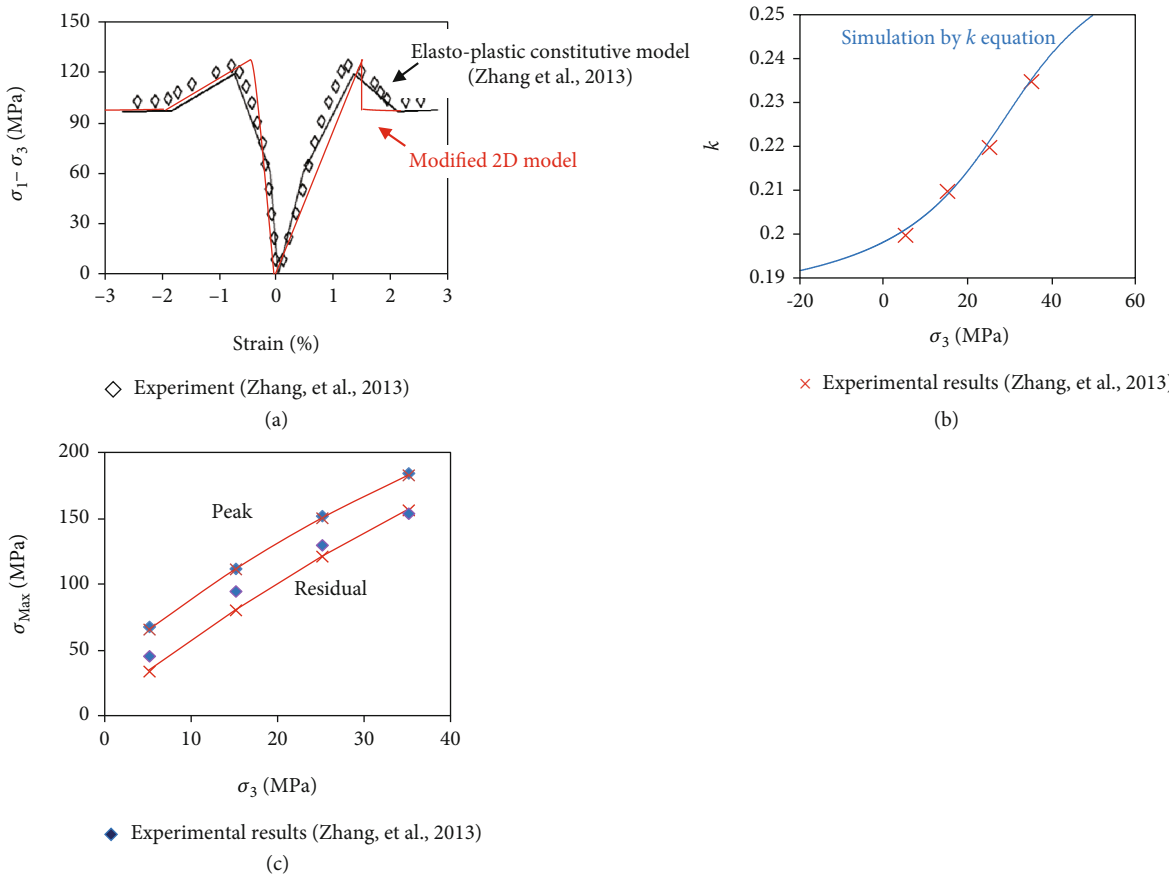

Figure 15: (a) Stress-strain curves of red sandstone under $\sigma_3 = 25$ (MPa). (b) k vs. σ_3 for parameter $A = 9$ (GPa), $C = 2.5$, and $\varepsilon_s = 0.002$. (c) Approximated convex failure envelopes by modified 2D model.

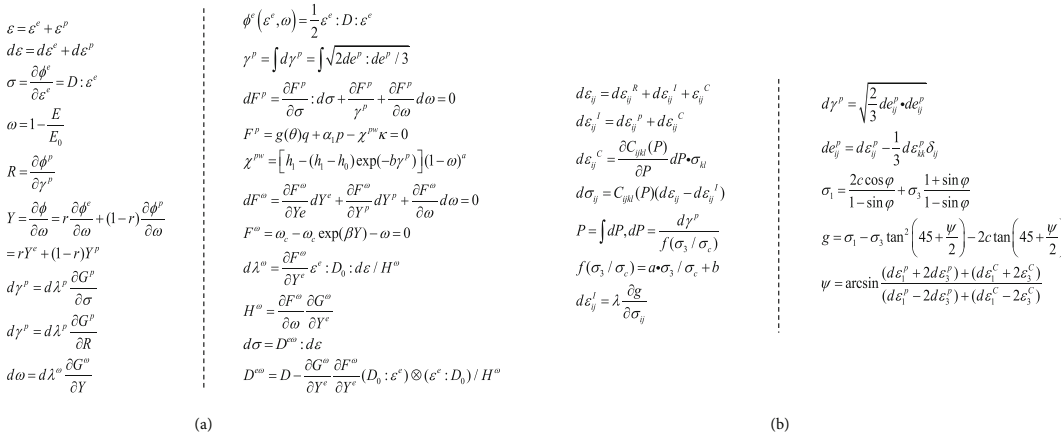

Figure 16: (a) A 2D conventional elasto-plastic constitutive model [12]. (b) Another example [13].

The stress–strain curves and convex failure envelopes for two types rocks, limestone and red sandstone [12, 13], are approximated by the modified 2D model. For limestone, the parameters $A = 27$ GPa, $C = 3.5$, and $\varepsilon_s = 0.0013$ were given, and the parameters $k_0 = 0.143$, $\Delta k = 0.0239$, $\alpha = 2.04$ MPa, and $\sigma_0 = 20.9$ MPa were obtained by a nonlinear least-squares method (Figure 14(b)). For red sandstone, the parameters $A = 9$ GPa, $C = 2.5$, and $\varepsilon_s = 0.002$ were given, and the parameters $k_0 = 0.18$, $\Delta k = 0.0928$, $\alpha = 20.6$ MPa, and $\sigma_0 = 29.0$ MPa were obtained by a nonlinear least-squares method (Figure 15(b)). The stress–strain curves (Figures 14(a) and 15(a)) and convex failure envelopes (Figures 14(c) and 15(c)) for rocks are simulated well.

3.3. Comparison with Other 2D Models. For comparison, we discuss the examples of two conventional 2D elasto-plastic constitutive models (Figure 16(a), [12]; Figure 16(b), [13]). These models are complicated and need 11 and 10

Downloaded from http://pubs.geoscienceworld.org/gsa/lithosphere/article-pdf/doi/10.2113/2022/1409110/5686341/1409110.pdf
by guest

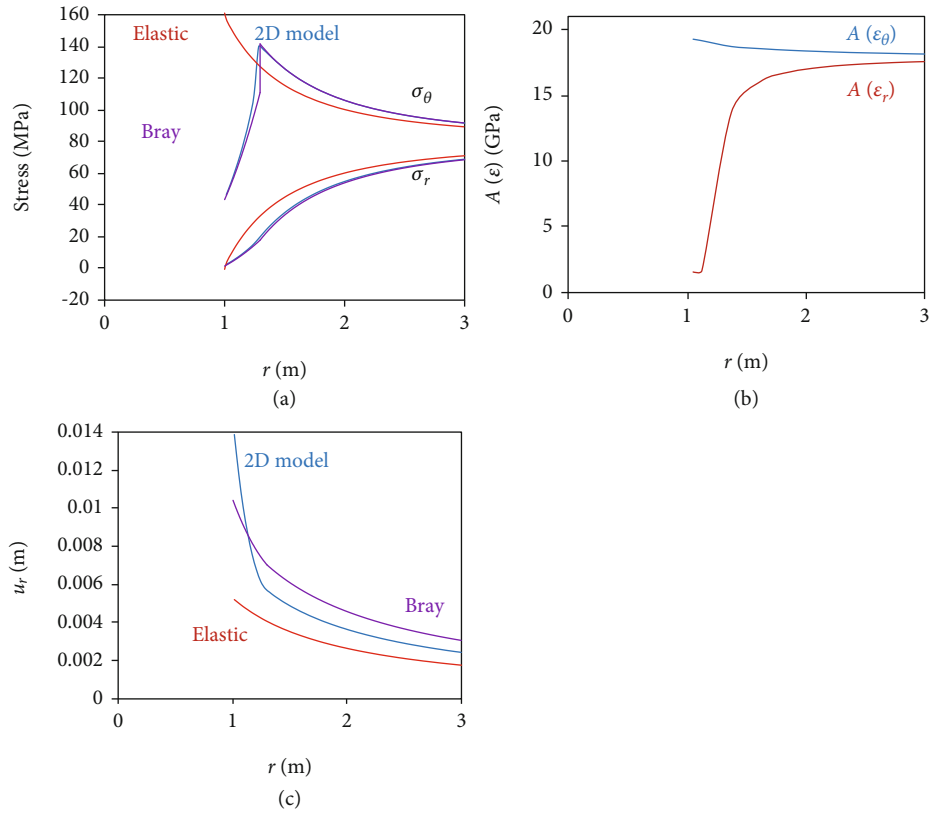

FIGURE 17: Calculation results for a hollow cylinder. Parameters for the simple 2D model and that for Bray's analytical elasto-plastic solution are the same as for Figure 10(a) ($A = 20$ (GPa), $k = 0.25$, $C = 1$, and $\varepsilon_s = 0.002$); $P_1 = 1$ (MPa) and $P_2 = 80$ (MPa). u_r is the inward displacement by excavation and application of P_1. (a) Stress distribution. (b) A (ε_r) and A (ε_θ). (c) Inward displacement.

parameters, respectively, to approximate the experimental stress–strain curves.

The results according to Zhang [12], including elastic ($E_0 = 45.51$ GPa and $\nu_0 = 0.320$), strength ($\alpha_1 = 2.07$, $\kappa = 34.5$ MPa, and $\alpha_2 = 2.07$), plastic hardening ($h_0 = 0.58$, $h_1 = 1.40$, and $b = 900$), damage ($\omega_c = 0.70$, $\beta_1 = 0.50$ MPa^{-1}, and $r = 0.2$), and damage softening ($a = 3.45$ exp $[-0.047\sigma_3]$) parameters, are represented by the blue lines in Figure 14(a).

The results according to Zhang, et al. [13], including elastic (bulk modulus, $K_0 = 8$ GPa; shear modulus initial value, $G_0 = 6$ GPa; shear modulus residual value, $G_r = G_0 \times 0.8$) and plastic (friction angle plastic internal variable threshold, $P_\phi = 0.4$; friction angle initial value, $\phi_0 = 18°$; friction angle residual value, $\phi_r = 34.5°$; shear dilatancy angle initial value, $\psi_0 = 25°$; shear dilatancy angle residual value, $\psi_r = 10°$; cohesion initial value $c_0 = 15$ MPa; cohesion residual value $c_r = 9.0$ MPa) parameters, and a plastic internal variable ($2.5\sigma_3/\sigma_c + 0.27$) are represented by the black lines in Figure 15(a).

The two models simulate the experimental stress–strain curves well. However, the models can neither simulate tensile failure nor consider the critical strains, and they both approximate failure envelopes as linear.

Among these three models, the modified 2D model is the best because it can approximate the stress–strain curves as precisely as the others, but can approximate convex failure envelope and uses fewer equations and parameters.

3.4. Example Application. As an example of its application, we calculated the stress distribution of a pressurized thick-walled cylinder with inner and outer radii $r_1 = 1$ m and $r_2 = 100$ m, respectively, under internal and external pressures $P_1 = 1$ MPa and $P_2 = 80$ MPa, respectively, using the simple 2D model and assuming the plane strain condition. The calculation was carried out by an axisymmetric finite element method (FEM), dividing the radial axis from 1 to 19 m into 470 elements, and from 19 to 100 m into 320 elements. The results were compared to Bray's analytical elasto-plastic solution [50] for a circular hole in an infinite elasto-brittle material (Figure 1(c)). The modified 2D model was not used because Bray's solution was only for a linear failure envelope and thus cannot be compared.

Parameters that were the same as for Figures 10(a) and 10(f) ($A = 20$ GPa, $k = 0.25$, $C = 1$, and $\varepsilon_s = 0.002$) and were used for the simple 2D model. The uniaxial compressive strength $q_u = 71.4$ MPa, internal friction angle $\phi = 36.5°$, friction angle for the residual strength $\phi' = 36.9°$, $E = 14.5$ GPa, $\nu = 0.270$, and residual cohesion $S_j = 9.89$ MPa were used for Bray's solution. The parameters are obtained from Figures 10(a)–10(f).

Downloaded from http://pubs.geoscienceworld.org/gsa/lithosphere/article-pdf/doi/10.2113/2022/1409110/5686341/1409110.pdf
by guest

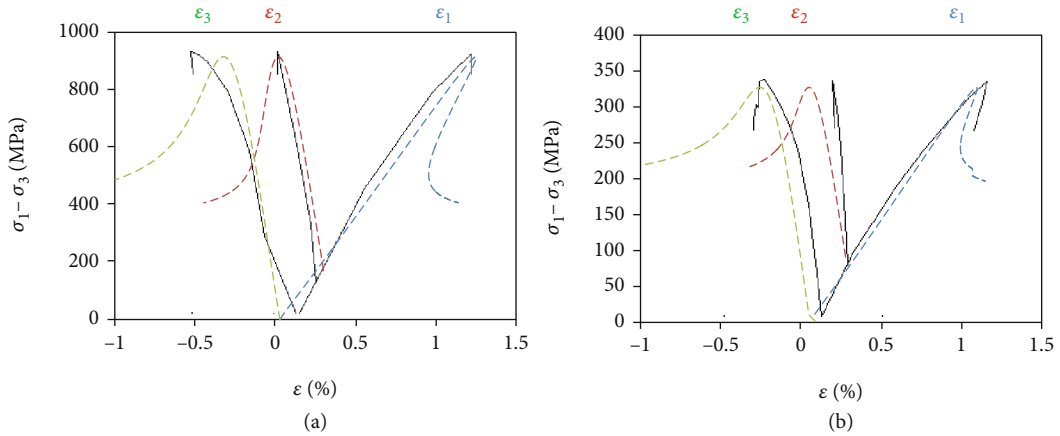

FIGURE 18: Stress strain curves under (a) $\sigma_2 = 300$ (MPa) and $\sigma_3 = 100$ (MPa) for KTB amphibolite [28] and (b) $\sigma_2 = 125$ (MPa) and $\sigma_3 = 50$ (MPa) for Coconino sandstone [29]. The dashed/solid lines are the simulated/experimental results.

Plastic zones can be seen for both models (Figure 17(a)). The decrease in strain-dependent elastic modulus (Figure 17(b)) around the opening induced a tangential stress decrease for the simple 2D model. The results from Bray's solution appear somewhat angular when plotted, while the results of the simple 2D model are more rounded, reflecting the difference in the stress–strain relationship. The inward displacement by the simple 2D model (Figure 17(c)) rapidly increases near the inner wall. This rapid increase may represent the dilatancy of rock failure better than Bray's solution, which is based on the rupture plane slip in the plastic zone.

4. Simple 3D Model

We propose the following simple 3D constitutive model:

$$\sigma_1 = A(\varepsilon_1)\varepsilon_1 + \mathrm{kA}\varepsilon_2 + \mathrm{kA}\varepsilon_3, \tag{21}$$

$$\sigma_3 = \mathrm{kA}\varepsilon_1 + \mathrm{kA}\varepsilon_2 + A(\varepsilon_3)\varepsilon_3, \tag{22}$$

$$\varepsilon_2 = \frac{\sigma_1 - \sigma_2}{\sigma_1 - \sigma_3}\varepsilon_3 + \frac{\sigma_2 - \sigma_3}{\sigma_1 - \sigma_3}\varepsilon_1. \tag{23}$$

Equations (21) and (22) are based on Equations (14) and (15) for the 2D model. Equation (23) is just an elastic equation. The same strain-dependent elastic modulus $A'(\varepsilon)$ is used as in Equation (16):

$$A'(\varepsilon) = D\left[\tan^{-1}\left\{C\left(\frac{\varepsilon}{\varepsilon_s} + 1\right)\right\} + \frac{\pi}{2}\right] + F, \tag{24}$$

and the terms D and F are chosen so that the residual strength becomes constant for infinite axial compression and lateral expansion (similar to the 2D model) as follows.

Let us assume

$$A'(\varepsilon_1 = \infty) = A. \tag{25}$$

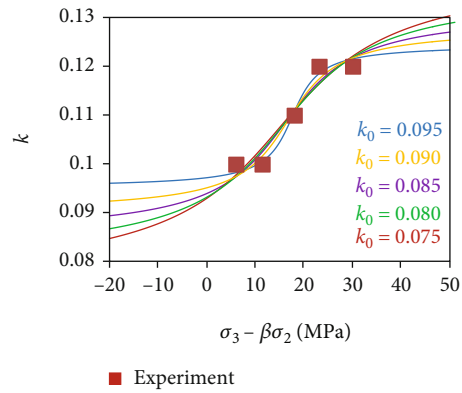

FIGURE 19: Example of k vs. $\sigma_3 - \beta\sigma_2$ for Westerly granite [51] for $A = 58.5$ (GPa), $C = 2$, $\varepsilon_s = 0.0007$, and $\beta = 0.7$. The fitting lines were obtained by a nonlinear least-squares method. $k_0 = 0.085$ gave the best results in the case.

As ε_3 tends to $-\infty$,

$$A'(\varepsilon_3 = -\infty) = F. \tag{26}$$

Substituting Equations (25) and (26) into Equations (21) and (22),

$$\sigma_3(\varepsilon_1 = \infty, \varepsilon_3 = -\infty) = F\varepsilon_3 + \mathrm{kA}\left(\frac{\sigma_1 - \sigma_2}{\sigma_1 - \sigma_3}\varepsilon_3 + \frac{\sigma_2 - \sigma_3}{\sigma_1 - \sigma_3}\varepsilon_1\right) + \mathrm{kA}\varepsilon_1, \tag{27}$$

$$\sigma_1(\varepsilon_1 = \infty, \varepsilon_3 = -\infty) = A\varepsilon_1 + \mathrm{kA}\left(\frac{\sigma_1 - \sigma_2}{\sigma_1 - \sigma_3}\varepsilon_3 + \frac{\sigma_2 - \sigma_3}{\sigma_1 - \sigma_3}\varepsilon_1\right) + \mathrm{kA}\varepsilon_3. \tag{28}$$

Downloaded from http://pubs.geoscienceworld.org/gsa/lithosphere/article-pdf/doi/10.2113/2022/1409110/5686341/1409110.pdf
by guest

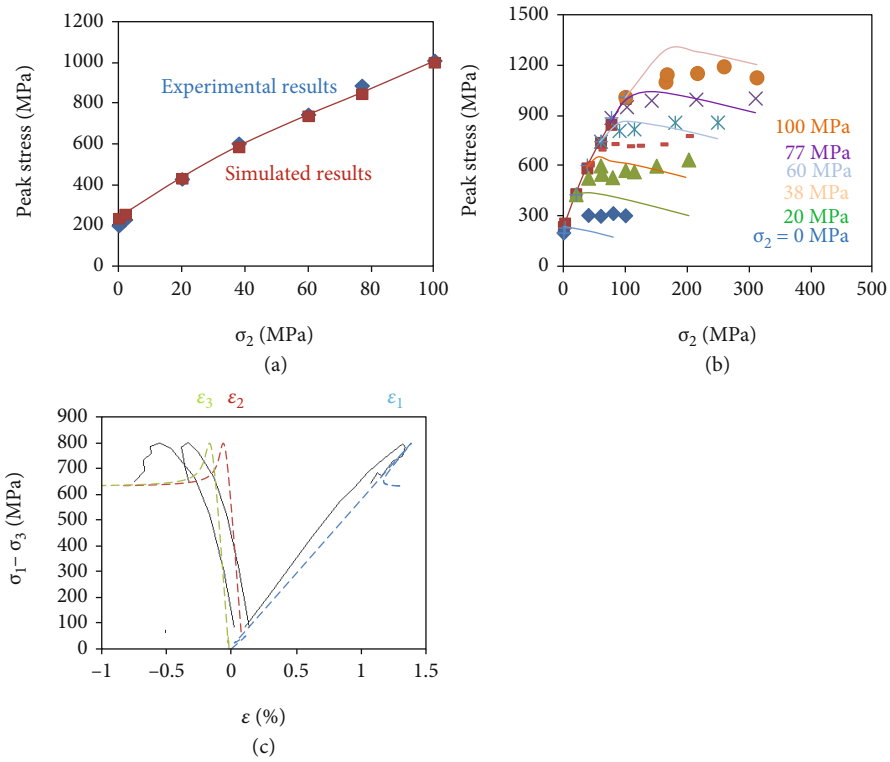

FIGURE 20: Approximation by the modified 3D model for Westerly granite by parameters $A = 58.5$ (GPa), $C = 2$, $\varepsilon_s = 0.0007$, $\alpha = 11.05$ (MPa), $\sigma_0 = 16.01$ MPa, $\Delta k = 0.0467$, and $k_0 = 0.085$. (a) Failure envelope for $\sigma_2 = \sigma_3$. (b) Failure envelope for $\sigma_2 > \sigma_3$. The lines/symbols were simulated/experimental results by 3D equations ([51]). (c) Example of true stress strain curves for $\sigma_2 = 114$ (MPa) and $\sigma_3 = 60$ (MPa). The dashed/solid lines are the simulated/experimental results.

Substituting Equation (27) into Equation (28),

$$\sigma_1(\varepsilon_1 = \infty, \varepsilon_3 = -\infty) = H\varepsilon_1 + \frac{\mathrm{kA}(1 + (\sigma_1 - \sigma_2)/(\sigma_1 - \sigma_3))}{\mathrm{kA}(\sigma_1 - \sigma_2)/(\sigma_1 - \sigma_3) + F}\sigma_3, \tag{29}$$

where

$$H = A + \mathrm{kA}\frac{\sigma_2 - \sigma_3}{\sigma_1 - \sigma_3} - \frac{k^2A^2(1 + (\sigma_1 - \sigma_2)/(\sigma_1 - \sigma_3))}{\mathrm{kA}(\sigma_1 - \sigma_2)/(\sigma_1 - \sigma_3) + F} \cdot \left(1 + \frac{\sigma_2 - \sigma_3}{\sigma_1 - \sigma_3}\right). \tag{30}$$

Assuming $\sigma_1(\varepsilon_1 = \infty, \varepsilon_3 = -\infty) = \text{const.}$, H should be 0,

$$F = \frac{k(1 + (\sigma_1 - \sigma_2)/(\sigma_1 - \sigma_3))(1 + (\sigma_2 - \sigma_3)/(\sigma_1 - \sigma_3)) - (\sigma_1 - \sigma_2)/(\sigma_1 - \sigma_3)(1 + k(\sigma_2 - \sigma_3)/(\sigma_1 - \sigma_3))}{1 + k(\sigma_1 - \sigma_2)/(\sigma_1 - \sigma_3)}\mathrm{kA}, \tag{31}$$

$$D = \frac{A - F}{\pi}. \tag{32}$$

For example, the simulation procedure for stress–strain curves becomes

(c1) Assign negative ε_3 increment
(c2) Calculate $A^{'}(\varepsilon)$ by Equation (24)
(c3) Calculate ε_1 by Equation (22)
(c4) Calculate σ_1 by Equation (21)
(c5) Iterate steps (c2–c4) until convergence
(c6) Calculate ε_2 by Equation (23)
(c7) Iterate steps (c1–c6) until ε_3 reaches -0.045

We approximated the true triaxial compression data under $\sigma_2 = 300$ (MPa) and $\sigma_3 = 100$ (MPa) for Cretaceous–Tertiary boundary (KTB) amphibolite [28] and under $\sigma_2 = 125$ MPa and $\sigma_3 = 50$ MPa for Coconino sandstone [29]. The approximation procedure is the same as steps (b1–b5). The results (Figure 18) is approximated well by the simple 3D model. This model requires only four

Downloaded from http://pubs.geoscienceworld.org/gsa/lithosphere/article-pdf/doi/10.2113/2022/1409110/5686341/1409110.pdf
by guest

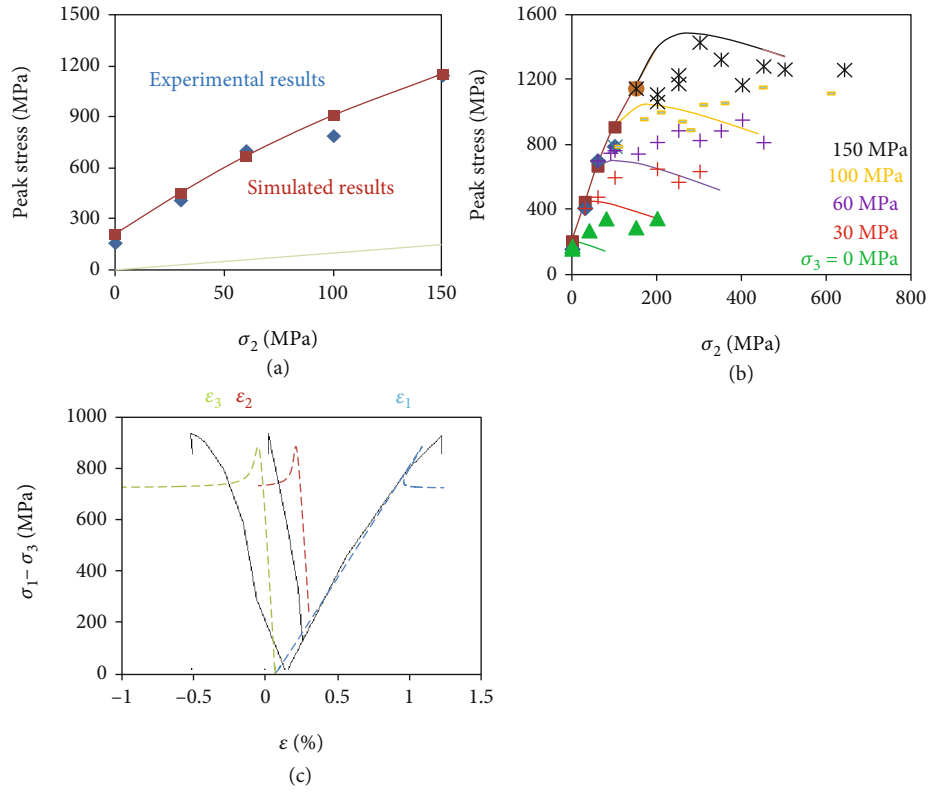

FIGURE 21: Approximation by the modified 3D model for KTB amphibolite by parameters A =90 (GPa), $C = 2$, $\varepsilon_s = 0.0005$, $\alpha = 24.8$ (MPa), $\sigma_0 = 33.2$ MPa, $\Delta k = 0.0792$, and $k_0 = 0.1$. (a): Failure envelope for $\sigma_2 = \sigma_3$. (b): Failure envelope for $\sigma_2 > \sigma_3$. The lines/symbols were calculated/experimental results by 3D equations/[28]. (c): Example of true stress strain curves for $\sigma_2 = 300$ (MPa) and σ_3 =100 (MPa). The dashed/solid lines are the simulated/experimental results.

parameters ($A = 90$ GPa, $C = 2$, $\varepsilon_s = 0.0035$, and $k = 0.22$ for Figure 18(a); $A = 37.5$ GPa, $C = 1.5$, $\varepsilon_s = 0.0025$, and $k = 0.217$ for Figure 18(b)). However, the peak stress–σ_2 relationship is not considered in this model; this is one of its limitations. We introduce stress-dependent k in the next chapter to approximate the convex peak stress–σ_2 relationship.

5. Modified 3D Model

5.1. Introduction of Stress-Dependent k. We now introduce stress-dependent k (Figure 19), with an additional term $-\beta\sigma_2$ compared to Equation (20):

$$k = \frac{\Delta k}{\pi}\left[\tan^{-1}\left\{\frac{1}{\alpha}(\sigma_3 - \beta\sigma_2 - \sigma_0)\right\} + \frac{\pi}{2}\right] + k_0, \qquad (33)$$

where β is a constant to adjust the effect of σ_2, taking a value between 0 (no effect) and 1 (the same effect as σ_3).

For example, the calculation procedure for stress–strain curves becomes

(d1) Assign negative ε_3 increment
(d2) Calculate $A'(\varepsilon)$ by Equation (24)
(d3) Calculate ε_1 by Equation (22)
(d4) Calculate σ_1 by Equation (21)
(d5) Calculate ε_2 by Equation (23)
(d6) Calculate k by Equation (33)
(d7) Iterate steps (d2–d6) until k converges
(d8) Iterate steps (d1–d7) for loading until ε_3 reaches -0.045

5.2. Prediction of σ_2 Effects. In chapter 4, the true stress–strain curves of KTB amphibolite [28] and Coconino sandstone [29] were simulated well by the 3D constitutive model for specific values of σ_2 and σ_3. We then approximated the stress–strain curves and peak stress–σ_2 relationship for Westerly granite [51] and the two rocks above using the modified 3D model. The following steps are added to the approximation steps above (b1–b5):

(e6) Assume β at 0.3, 0.5, 0.7, and 0.9
(e7) Obtain k vs. $\sigma_3 - \beta\sigma_2$ curve for $\sigma_2 = \sigma_3$
(e8) Assume k_0 (e.g., 0.075, 0.080, 0.085, 0.090, and 0.095 for Westerly granite)
(e9) Obtain values of Δk, α, and σ_s by a nonlinear least-squares method (e.g., Figure 19)
(e10) Calculate stress–strain curves and failure envelopes
(e11) Iterate steps (e8–e10)
(e12) Iterate steps (e6–e11)
(e13) Select a set of parameters that can best simulate the peak stress–σ_2 curve under $\sigma_2 > \sigma_3$

An example plot of k vs. $\sigma_3 - \beta\sigma_2$ for Westerly granite with $\beta = 0.7$ is shown in Figure 19. The parameter values were obtained for each k_0 by a nonlinear least-squares method. The failure envelopes of all rock types for $\sigma_2 = \sigma_3$ (Figures 20(a), 21(a), and 22(a)) were approximated

Downloaded from http://pubs.geoscienceworld.org/gsa/lithosphere/article-pdf/doi/10.2113/2022/1409110/5686341/1409110.pdf
by guest

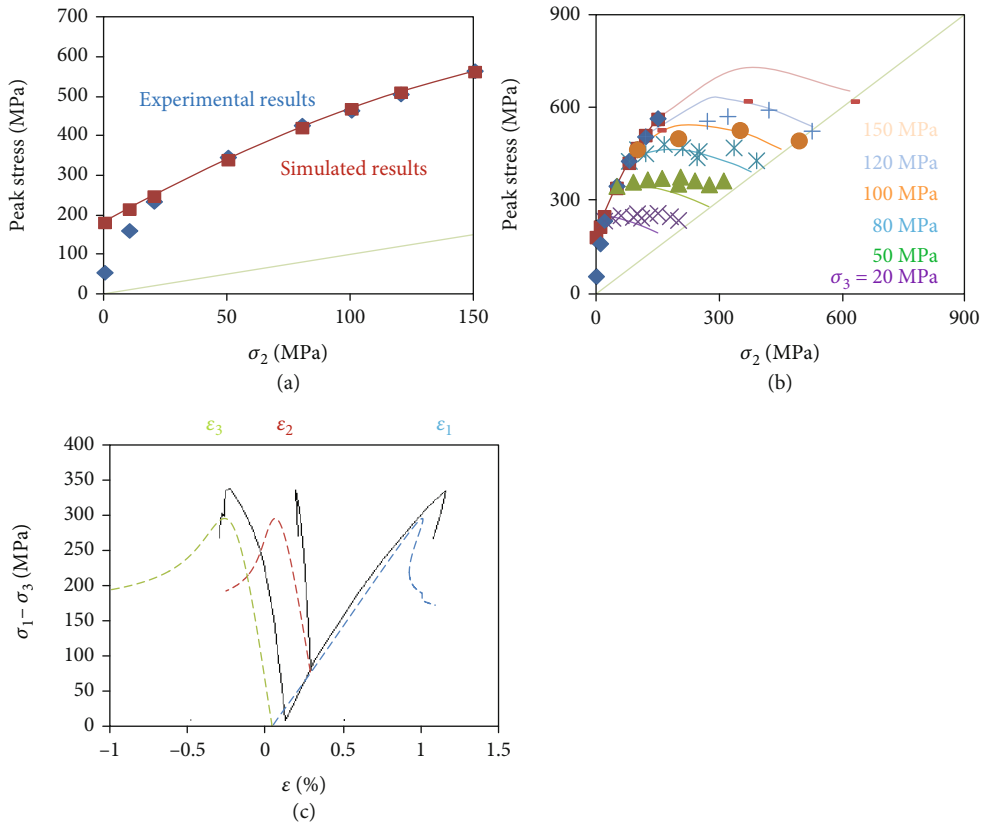

Figure 22: Approximation by the modified 3D model for sandstone by parameters $A = 37.5$ (GPa), $C = 1.5$, $\varepsilon_s = 0.0025$, $\alpha = 54.5$ (MPa), $\sigma_0 = 86.0$ MPa, $\Delta k = 0.702$, and $k_0 = 0.14$. (a): Failure envelope for $\sigma_2 = \sigma_3$. (b): Failure envelope for $\sigma_2 > \sigma_3$. The lines/symbols were calculated/experimental results by 3D equations/[29]. (c): Example of true stress strain curves for $\sigma_2 = 125$ (MPa) and $\sigma_3 = 50$ (MPa). The dashed/solid lines are the simulated/experimental results.

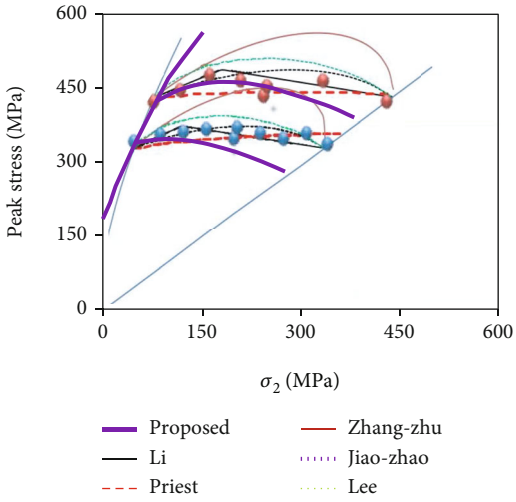

Figure 23: The peak stress-σ_2 relationship for sandstone. The symbols were experimental results by [29].

reasonably well. The true stress–strain curves of rock (Figures 20(c), 21(c), and 22(c)) under the modified 3D model were somewhat different from those under the simple 3D model (Figure 18), because the former prioritized approximating the failure envelope. For Westerly granite and KTB amphibolite, the failure envelope for $\sigma_2 > \sigma_3$ at high σ_3 was simulated well, while the modified 3D model underestimates the peak stress at low σ_3 (Figures 20(b) and 21(b)). For sandstone, this model simulated the failure envelope well for $\sigma_2 > \sigma_3$ at low σ_3, while it overestimates the peak stress at high σ_3 (Figure 22(b)).

5.3. Comparison with Other 3D Criteria. In Figure 23, we show a comparison of 3D failure criteria ([36, 40, 41, 43, 52], and [38]) from Li et al. [38]. In this figure, we have also plotted the peak stress–σ_2 relationship according to the modified 3D model in chapter 5.2. Some of these criteria give better results than the proposed model; however, they do not give a reasonable nonlinear stress–strain relationship. Therefore, it is better to use one of these criteria when the stress–strain relationship is almost linear, and it is important that the failure envelope be followed strictly. However, it is better to use our proposed model to represent nonlinear stress–strain relationships well while following the true triaxial failure envelope.

6. Concluding Remarks

To propose a 3D constitutive model for rocks, with fewer parameters and consideration of true triaxial stress–strain curves and convex failure envelopes, we first modified the simple 2D model previously proposed by our research group

Downloaded from http://pubs.geoscienceworld.org/gsa/lithosphere/article-pdf/doi/10.2113/2022/1409110/5686341/1409110.pdf
by guest

to have a convex failure criterion. The effects of the parameters on the failure envelope were observed, and a procedure to approximate the stress–strain curves and failure envelopes was proposed. This model approximated these well (much better than conventional 2D models). The new 2D model was applied to a pressurized thick-walled cylinder under the plane strain condition.

The simple 2D constitutive model was then extended to a simple 3D model. True triaxial stress–strain curves under specific values of σ_2 and σ_3 were approximated reasonably. However, the predicted peak stress–σ_2 relationship was linear.

Finally, the 3D model was developed by introducing stress-dependent k. Under this, the peak stress–σ_2 relationship for true triaxial compression first increased and then decreased with σ_2, as occurs in actual rocks. True triaxial stress–strain curves and failure envelopes were simulated reasonably.

This modified 3D model is the only one that can fairly represent the true triaxial nonlinear stress–strain curves and convex failure envelopes. Combining it with a 3D finite element method could improve the design of rock structures.

Data Availability

Some or all data, models, or code that support the findings of this study are available from the corresponding author upon reasonable request.

Conflicts of Interest

We declare there is no conflict of interest.

Acknowledgments

This research was supported by the Ministry of Education, Culture, Sports, Science, and Technology of Japan and the China Scholarship Council.

References

[1] D. L. Cecilio, P. R. B. Devloo, S. M. Gomes, E. R. S. dos Santos, and N. Shauer, "An improved numerical integration algorithm for elastoplastic constitutive equations," *Computers and Geotechnics*, vol. 64, pp. 1–9, 2015.

[2] N. Cristescu, "Elastic/viscoplastic constitutive equations for rock," *International Journal of Rock Mechanics and Mining Sciences & Geomechanics Abstracts*, vol. 24, no. 5, pp. 271–282, 1987.

[3] N. Cristescu and U. Hunsch, "Determination of nonassociated constitutive equation for rock salt from experiments," *Finite Inelastic Deformations—Theory and Applications*, vol. 1991, pp. 511–523, 1991.

[4] G. Frantziskonis and C. S. Desai, "Constitutive model with strain softening," *International Journal of Solids and Structures*, vol. 23, no. 6, pp. 733–750, 1987.

[5] M. Ismael and H. Konietzky, "Constitutive model for inherent anisotropic rocks: ubiquitous joint model based on the hoek-brown failure criterion," *Computers and Geotechnics*, vol. 105, pp. 99–109, 2019.

[6] C. Li, R. Prikryl, and E. Nordlund, "The stress-strain behaviour of rock material related to fracture under compression," *Engineering Geology*, vol. 49, no. 3-4, pp. 293–302, 1998.

[7] S. Okubo and K. Fukui, "An analytical investigation of a variable-compliance-type constitutive equation," *Rock Mechanics and Rock Engineering*, vol. 39, no. 3, pp. 233–253, 2006.

[8] O. Pourhosseini and M. Shabanimashcool, "Development of an elasto-plastic constitutive model for intact rocks," *International Journal of Rock Mechanics and Mining Sciences*, vol. 66, pp. 1–12, 2014.

[9] S. Wang, W. Xu, W. Wang, and C. Jia, "Experimental and numerical investigations on the mechanical behavior of fine-grained sandstone," *International Journal of Geomechanics*, vol. 18, no. 2, article 04017150, 2018.

[10] M. C. Weng, F. S. Jeng, Y. M. Hsieh, and T. H. Huang, "A simple model for stress-induced anisotropic softening of weak sandstones," *International Journal of Rock Mechanics and Mining Sciences*, vol. 45, no. 2, pp. 155–166, 2008.

[11] N. Xie, Q. Z. Zhu, L. H. Xu, and J. F. Shao, "A micromechanics-based elastoplastic damage model for quasi-brittle rocks," *Computers and Geotechnics*, vol. 38, no. 8, pp. 970–977, 2011.

[12] J. C. Zhang, "Experimental and modelling investigations of the coupled elastoplastic damage of a quasi-brittle rock," *Rock Mechanics and Rock Engineering*, vol. 51, no. 2, pp. 465–478, 2018.

[13] K. Zhang, H. Zhou, and J. Shao, "An experimental investigation and an elastoplastic constitutive model for a porous rock," *Rock Mechanics and Rock Engineering*, vol. 46, no. 6, pp. 1499–1511, 2013.

[14] S. Q. Yang, H. W. Jing, and S. Y. Wang, "Experimental investigation on the strength, deformability, failure behavior and acoustic emission locations of red sandstone under triaxial compression," *Rock Mechanics and Rock Engineering*, vol. 45, no. 4, pp. 583–606, 2012.

[15] D. K. Hallbauer, H. Wagner, and N. G. W. Cook, "Some observations concerning the microscopic and mechanical behaviour of quartzite specimens in stiff, triaxial compression tests," *International Journal of Rock Mechanics and Mining Sciences & Geomechanics Abstracts*, vol. 10, no. 6, pp. 713–726, 1973.

[16] C. D. Martin and N. A. Chandler, "Stress heterogeneity and geological structures," *International Journal of Rock Mechanics and Mining Sciences & Geomechanics Abstracts*, vol. 30, no. 7, pp. 993–999, 1993.

[17] N. Cho, C. D. Martin, and D. C. Sego, "A clumped particle model for rock," *International Journal of Rock Mechanics and Mining Sciences*, vol. 44, no. 7, pp. 997–1010, 2007.

[18] E. Z. Lajtai, "Microscopic fracture processes in a granite," *Rock Mechanics and Rock Engineering*, vol. 31, no. 4, pp. 237–250, 1998.

[19] W. R. Wawersik and C. Fairhurst, "A study of brittle rock fracture in laboratory compression experiments," *International Journal of Rock Mechanics and Mining Sciences & Geomechanics Abstracts*, vol. 7, no. 5, pp. 561–575, 1970.

[20] Y. Fujii, T. Kiyama, Y. Ishijima, and J. Kodama, "Examination of a rock failure criterion based on circumferential tensile strain," *Pure and Applied Geophysics*, vol. 152, no. 3, pp. 551–577, 1998.

[21] M. Singh and B. Singh, "High lateral strain ratio in jointed rock masses," *Engineering Geology*, vol. 98, no. 3-4, pp. 75–85, 2008.

[22] Y. Fujii and Y. Ishijima, "Simple Constitutive Equations for Brittle Rocks, Based on Strain-Dependent Stiffness," in

Downloaded from http://pubs.geoscienceworld.org/gsa/lithosphere/article-pdf/doi/10.2113/2022/1409110/5686341/1409110.pdf
by guest

Advances in Rock Mechanics, Y. Lin, Ed., pp. 186–193, World Scientific Publishing, Singapore, New Jersey, London, Hong Kong, 1998.

[23] Y. Fujii and Y. Ishijima, "Constitutive equations for rock, based in radial stiffness decrease," *Shigen-to-Sozai*, vol. 114, no. 3, pp. 169–174, 1998.

[24] S. A. F. Murrell, "The effect of triaxial stress systems on the strength of rocks at atmospheric temperatures," *Geophysical Journal International*, vol. 10, no. 3, pp. 231–281, 1965.

[25] K. Mogi, "Effect of the intermediate principal stress on rock failure," *Journal of Geophysical Research*, vol. 72, no. 20, pp. 5117–5131, 1967.

[26] K. Mogi, "Effect of the triaxial stress system on the failure of dolomite and limestone," *Tectonophysics*, vol. 11, no. 2, pp. 111–127, 1971.

[27] K. Mogi, "Fracture and flow of rocks under high triaxial compression," *Journal of Geophysical Research*, vol. 76, no. 5, pp. 1255–1269, 1971.

[28] C. Chang and B. Haimson, "True triaxial strength and deformability of the German continental deep drilling program (KTB) deep hole amphibolite," *Journal of Geophysical Research*, vol. 105, no. B8, pp. 18999–19013, 2000.

[29] X. Ma and B. C. Haimson, "Failure characteristics of two porous sandstones subjected to true triaxial stresses," *Journal of Geophysical Research: Solid Earth*, vol. 121, no. 9, pp. 6477–6498, 2016.

[30] K. Mogi, *Experimental Rock Mechanics*, Taylor and Francis, London, 2007.

[31] S. Senent, R. Jimenez, and A. Reyes, "Numerical simulation of the influence of small-scale defects on the true- triaxial strength of rock samples," *Computers and Geotechnics*, vol. 53, pp. 142–156, 2013.

[32] M. You, "True-triaxial strength criteria for rock," *International Journal of Rock Mechanics and Mining Sciences*, vol. 46, no. 1, pp. 115–127, 2009.

[33] X. T. Feng, B. Haimson, X. C. Li et al., "ISRM suggested method: determining deformation and failure characteristics of rocks subjected to true triaxial compression," *Rock Mechanics and Rock Engineering*, vol. 52, no. 6, pp. 2011–2020, 2019.

[34] A. M. Al-Ajmi and R. W. Zimmerman, "Relation between the Mogi and the Coulomb failure criteria," *International Journal of Rock Mechanics and Mining Sciences*, vol. 42, no. 3, pp. 431–439, 2005.

[35] H. Jiang, X. W. Wang, and Y. L. Xie, "New strength criteria for rocks under polyaxial compression," *Canadian Geotechnical Journal*, vol. 48, no. 8, pp. 1233–1245, 2011.

[36] H. Jiang and J. Zhao, "A simple three-dimensional failure criterion for rocks based on the Hoek-Brown criterion," *Rock Mechanics and Rock Engineering*, vol. 48, no. 5, pp. 1807–1819, 2015.

[37] P. Lade and J. Duncan, "Elastoplastic stress–strain theory for cohesionless soil," *Journal of Geotechnical Engineering, ASCE*, vol. 101, no. 10, pp. 1037–1053, 1975.

[38] H. Li, T. Guo, Y. Nan, and B. Han, "A simplified three-dimensional extension of Hoek-Brown strength criterion," *Journal of Rock Mechanics and Geotechnical Engineering*, vol. 13, no. 3, pp. 568–578, 2021.

[39] N. Melkoumian, S. D. Priest, and S. P. Hunt, "Further development of the three-dimensional Hoek–Brown yield criterion," *Rock Mechanics and Rock Engineering*, vol. 42, no. 6, pp. 835–847, 2009.

[40] X. D. Pan and J. A. Hudson, "A simplified three dimensional Hoek–Brown yield criterion," in *Rock Mechanics and Power Plants*, M. Romana, Ed., pp. 95–103, Balkema, Rotterdam, 1988.

[41] S. D. Priest, "Determination of shear strength and three-dimensional yield strength for the Hoek-Brown criterion," *Rock Mechanics and Rock Engineering*, vol. 38, no. 4, pp. 299–327, 2005.

[42] L. Zhang, "A generalized three-dimensional Hoek–Brown strength criterion," *Rock Mechanics and Rock Engineering*, vol. 41, no. 6, pp. 893–915, 2008.

[43] L. Zhang and H. Zhu, "Three-dimensional Hoek-Brown strength criterion for rocks," *Journal of Geotechnical and Geoenviromental Engineering*, vol. 133, no. 9, pp. 1128–1135, 2007.

[44] R. Ewy, "Wellbore-stability predictions by use of a modified Lade criterion," *SPE Drilling & Completion*, vol. 14, no. 2, pp. 85–91, 1999.

[45] E. Hoek and E. T. Brown, "Empirical strength criterion for rock masses," *Journal of Geotechnical and Geoenviromental Engineering*, vol. 106, no. GT9, pp. 1013–1035, 1980.

[46] E. Hoek, C. Carranza-Torres, and B. Corkum, "Hoek-Brown Failure Criterion -2002 Edition," in *Proceeding of 5th North American Rock Mechanics Symposium and Tunneling Association of Canada Conference*, pp. 267–273, Toronto, 2002.

[47] S. L. Crouch and C. Fairhurst, *Mechanics of Coal Mine Bumps and the Interaction between Coal Pillars Mine Roof and Floor*, Department of Civil and Mineral Engineering, University of Minnesota, 1973.

[48] X. G. Zhao and M. Cai, "A mobilized dilation angle model for rocks," *International Journal of Rock Mechanics and Mining Sciences*, vol. 47, no. 3, pp. 368–384, 2010.

[49] H. Nishitani, *Computational and Experimental Fracture Mechanics*, Computational Mechanics Publications, Berlin, 1994.

[50] R. E. Goodman, *Introduction to Rock Mechanics*, John Wiley and Sons, 1980.

[51] B. C. Haimson and C. Chang, "A new true triaxial cell for testing mechanical properties of rock, and its use to determine rock strength and deformability of Westerly granite," *International Journal of Rock Mechanics and Mining Sciences*, vol. 37, no. 1-2, pp. 285–296, 2000.

[52] Y. K. Lee, S. Pietruszczak, and B. H. Choi, "Failure criteria for rocks based on smooth approximations to Mohr-Coulomb and Hoek-Brown failure functions," *International Journal of Rock Mechanics and Mining Sciences*, vol. 56, pp. 146–160, 2012.

Downloaded from http://pubs.geoscienceworld.org/gsa/lithosphere/article-pdf/doi/10.2113/2022/1409110/5686341/1409110.pdf
by guest